AGU PUBLICATIONS

JGR

Journal of Geophysical Research: Oceans

RESEARCH ARTICLE

10.1002/2015JC011314

Key Points:
- Generation of internal tide in a circular canyon
- Focusing of baroclinic tidal energy in canyon center
- Generation of a baroclinic eddy due to diapicnal mixing

Correspondence to:
V. Vlasenko,
vvlasenko@plymouth.ac.uk

Citation:
Vlasenko, V., N. Stashchuk, M. E. Inall, M. Porter, and D. Aleynik (2016), Focusing of baroclinic tidal energy in a canyon, *J. Geophys. Res. Oceans*, *121*, doi:10.1002/2015JC011314.

Received 21 SEP 2015
Accepted 1 APR 2016
Accepted article online 6 APR 2016

Focusing of baroclinic tidal energy in a canyon

Vasiliy Vlasenko[1], Nataliya Stashchuk[1], Mark E. Inall[2], Marie Porter[2], and Dmitry Aleynik[2]

[1]School of Marine Science and Engineering, University of Plymouth, Plymouth, UK, [2]Scottish Association for Marine Science, Scottish Marine Institute, Oban, UK

Abstract Strong three-dimensional focusing of internal tidal energy in the Petite Sole Canyon in the Celtic Sea is analyzed using observational data and numerical modeling. In a deep layer (500–800 m) in the center of the canyon, shear variance was elevated by an order of magnitude. Corresponding large vertical oscillations of deep isotherms and a local maximum of horizontal velocity were replicated numerically using the MITgcm. The elevated internal tidal activity in the deep part of the canyon is explained in terms of the downward propagation and focusing of multiple internal tidal beams generated at the shelf break. The near-circular shape of the canyon head and steep bottom topography throughout the canyon (steeper than the tidal beam) create favorable conditions for the lens-like focusing of tidal energy in the canyon's center. Observations and modeling show that the energy focusing greatly intensifies local diapycnal mixing that leads to local formation of a baroclinic eddy.

1. Introduction

Oceanic canyons are potential places for significant tidal energy conversion from the barotropic to baroclinic modes, with major implications for water mass mixing. According to *Hickey* [1995], nearly 20% of the Eastern Pacific shelf edge between Alaska and the equator is dominated by steep, narrow, and abrupt canyons. Historically, the first and most extensively studied canyon was La Jolla Canyon (California). The results by *Shepard* [1974] and *Gordon and Marshall* [1976] showed that steep canyons can act as a trap for tidally generated internal waves. Specifically, it was recognized that the dynamical processes occurring in canyons strongly depend on the ratio of the maximum bottom steepness ($S_{topo}=\partial H/\partial l$) (here $H(x,y)$ is the water depth, and l is the direction of the seabed depth gradient vector) to the inclination of the characteristic paths of the internal wave energy propagation

$$S_{wave}=dz/dl=\pm[(\omega^2-f^2)/(N^2(z)-\omega^2)]^{1/2}, \tag{1}$$

where ω is the tidal frequency, f is the Coriolis parameter, and $N(z)$ is the buoyancy frequency. In other words, in terms of the mechanism of internal wave dynamics, the following parameter

$$\alpha(x,y,z)=\frac{S_{topo}}{S_{wave}}=\frac{|\partial H/\partial l|}{[(\omega^2-f^2)/(N^2(z)-\omega^2)]^{1/2}}, \tag{2}$$

is the principal measure of the bottom steepness that distinguishes two very different regimes of tidal energy conversion. Schematically they are presented in Figure 1. For specificity, the buoyancy frequency measured in a canyon of the Celtic Sea (reported in *Vlasenko and Stashchuk* [2015]) is used for the analysis, see Figure 1a.

In a subcritical regime, when the condition $\alpha < 1$ is valid over the whole domain, it is mostly the lower tidal baroclinic modes that are generated. This regime is presented in Figure 1b.

Over "steep" topographies, for which $\alpha > 1$ occurs at least for some fragments of a given slope, the supercritical regime of tidal energy conversion, presented in Figure 1c (below point C), is fulfilled substantially increasing the conversion rate [*Gerkema et al*., 2004]. In this regime, internal tidal energy is concentrated in a narrow internal tidal beam (magenta stripe in Figure 1c) that radiates energy away from bottom fragments where $\alpha=1$. The energy propagates in the tidal beam upward and downward along characteristic line (1) with group velocity C_g while the wave phase propagates across the beam with the phase speed C_p, Figure 1c. In fact, it is not only the point C with $\alpha=1$ that is the area of the beam formation. A wider area

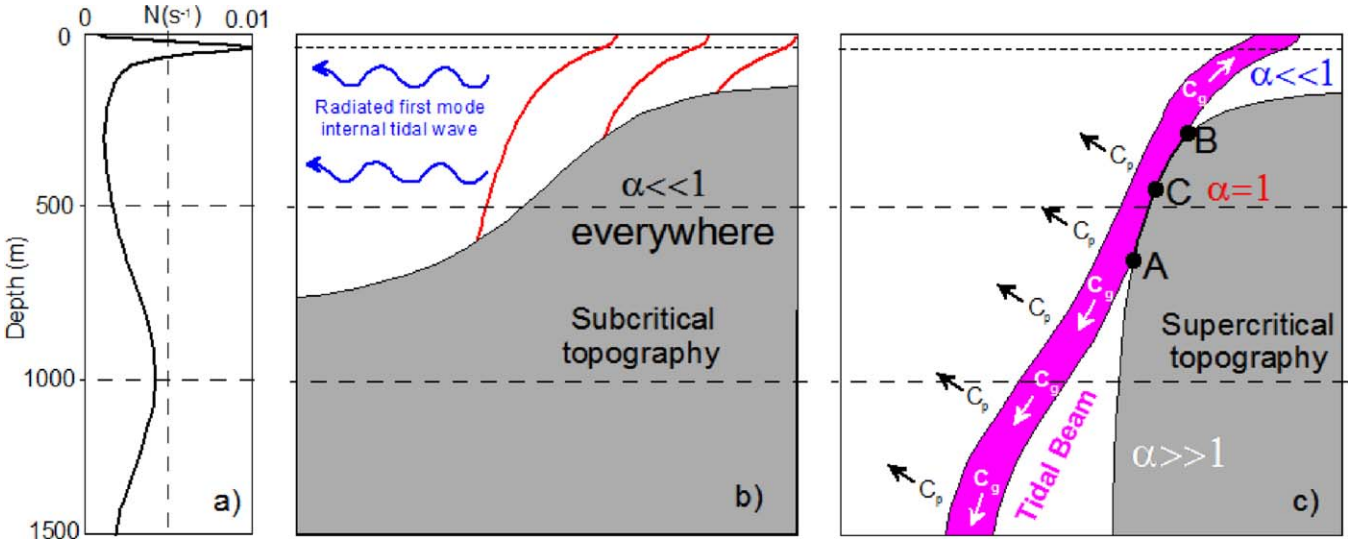

Figure 1. (a) Buoyancy frequency measured in the Celtic Sea. Schemes of the generation regime over (b) subcritical and (c) supercritical topographies. Red lines in Figure 1b show characteristics (1). Magenta area in Figure 1c depicts a tidal beam.

A-B where the bottom inclination is close to critical is the place of the beam generation. More on different regimes of tidal energy conversion can be found in *Vlasenko et al*. [2005].

Note that intensity of the tidal beam depends not only on the relative steepness of the bottom or strength of the tidal current. It is also controlled by smoothness of the buoyancy frequency profile. In highly intermittent media with sharp vertical changes of the buoyancy frequency, the downward propagated tidal energy is reflected back from the layered structures in the form of secondary tidal beams propagating to the free surface [*Grimshaw et al*., 2010]. This process can even lead to a complete attenuation of the tidal beam [*Gerkema and van Haren*, 2012]. However, as it was shown by *Vlasenko and Stashchuk* [2015], the surface 1.5 km layer of the Celtic Sea (which is in the focus of the present study) is mostly unaffected by internal reflection.

Note that the tidal beam is a superposition of many baroclinic modes, as it was clearly shown in the analytical solution for internal tides at abrupt topographies by *St. Laurent et al*. [2003], and the presence of a beam is evidence of higher mode excitation. For a typical "V"-shaped canyon with $\alpha \geq 1$, the baroclinic tidal energy is trapped inside the canyon, being able only to propagate downward reflecting many times from canyon's steep flanks without any opportunity of escape [see, for instance, *Balmforth and Peacock*, 2009, Figure 2].

The importance of the relative bottom steepness α for internal wave dynamics in canyons was acknowledged by *Petruncio et al*. [1998] in their interpretation of measurements conducted in another well-studied canyon, Monterrey Submarine Canyon. In further analysis by *Zhao et al*. [2012], who investigated the energetic characteristics of internal waves and turbulent mixing in the canyon, it was suggested that the topographic steepness does control the energy conversion rate.

Some studies on the baroclinic dynamics in canyons were conducted for an idealized bottom profiles by *Baines* [1983], *St. Laurent et al*. [2003], *Grimshaw et al*. [1985], and *Zhang et al*. [2014]. A more realistic model set up, specifically, the real bottom topography, was taken in a further series of numerical experiments performed for Monterey Submarine Canyon area: *Petruncio et al*. [2002] used POM, *Jachec et al*. [2006] operated with SUNTANS, and *Hall and Carter* [2011] used POM to investigate internal tides in the canyon area. However, the specific role of the relative steepness α of the canyon topography in the distribution of the baroclinic wave energy was not investigated in any of these studies. Specifically, the structure of the baroclinic tidal field in the areas where $\alpha > 1$, a common occurrence, has not hitherto been discussed in detail.

The purpose of this paper is to interpret the three-dimensional effects of internal tidal dynamics that are seen to occur in supercritical canyons. In particular, an original observational data set collected in a supercritical canyon in the Celtic Sea is analyzed here in terms of the focusing of internal tidal energy radiated from the areas with critical bottom inclination.

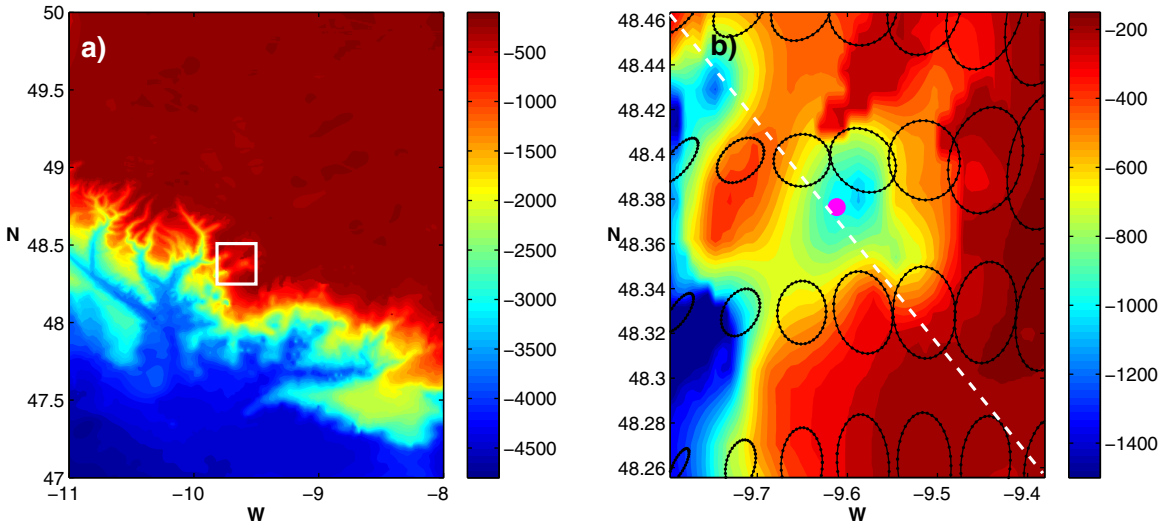

Figure 2. (a) Bathymetry of the Celtic Sea. White rectangle shows the position of the canyon. (b) Zoom of the Petite Sole Canyon area. The position of the yo-yo CTD station is depicted by a magenta dot. Tidal ellipses showing the intensity of the model forcing are presented by black contours.

2. Observations

The Celtic Sea is a 200 m deep, wide shelf sea with a large number of headlands and canyons along its shelf edge, Figure 2a. Observations analyzed here were conducted on the 376th cruise of the RRS "Discovery" (hereafter D376) in June 2012, as a part of the FASTNEt study to quantify the cross-shelf transport on the NE Atlantic Ocean margin. With relevance to this paper, 14 repeat "yo-yo" CTD profiles were conducted at a station precisely in the middle of the Petite Sole Canyon presented in Figure 2b. Vertical profiles were repeated with approximately 1 h time interval to the depth of approximately 1000 m. In addition to the CTD probe, a downward looking TRDI WHM 300 kHz LADCP was mounted on the frame, so that each CTD profile was accompanied by a vertical profile of currents.

All 14 "yo-yo" temperature profiles $T_j(z)$ ($j=1,2,3,\ldots,14$) are presented in Figure 3a by blue lines. The red line shows an equilibrium temperature distribution calculated as an average temperature at each depth. Comparing all individual temperature profiles $T_j(z)$ with the average $T(z)$, one can see that the largest deviations of every individual profile from the average take place in two zones: in the surface 150 m layer, and between 500 and 900 m depth. Assuming that these deviations were caused by the dynamical processes developing in the canyon, the vertical displacement ζ_j of every individual isotherm on every profile from the averaged temperature profile can be calculated using the following formula:

$$\zeta_j = \frac{|T_j - T|}{\partial T/\partial z}$$

An average profile of isotherms displacements, calculated as $1/14\sum_{j=1}^{14}\zeta_j(z)$, is presented in Figure 3b. It shows that the absolute maximum vertical displacements of isotherms, up to 45 m, are located in deep water, between 600 and 800 m depth. The deviation profile calculated as a maximum displacement of the isotherm from its equilibrium state is close to that shown in Figure 3b.

Note that the maximum baroclinic horizontal velocities at the "yo-yo" station were recorded by the LADCP in the surface layer [see also *Vlasenko et al.*, 2014]. However, Figure 3b suggests that a comparable contribution of the 600–800 m depth layer to the internal wave energy is also expected. In order to quantify the kinetic energy of dynamical processes developing at the "yo-yo" station, an average profile of horizontal velocities for all 14 LADCP sampling was calculated as follows

$$U(z) = 1/14\sum_{j=1}^{14}\sqrt{u_j^2(z)+v_j^2(z)}.$$

Here $u_j(z)$ and $v_j(z)$ ($j=1,2,\ldots,14$) are eastward and northward velocities.

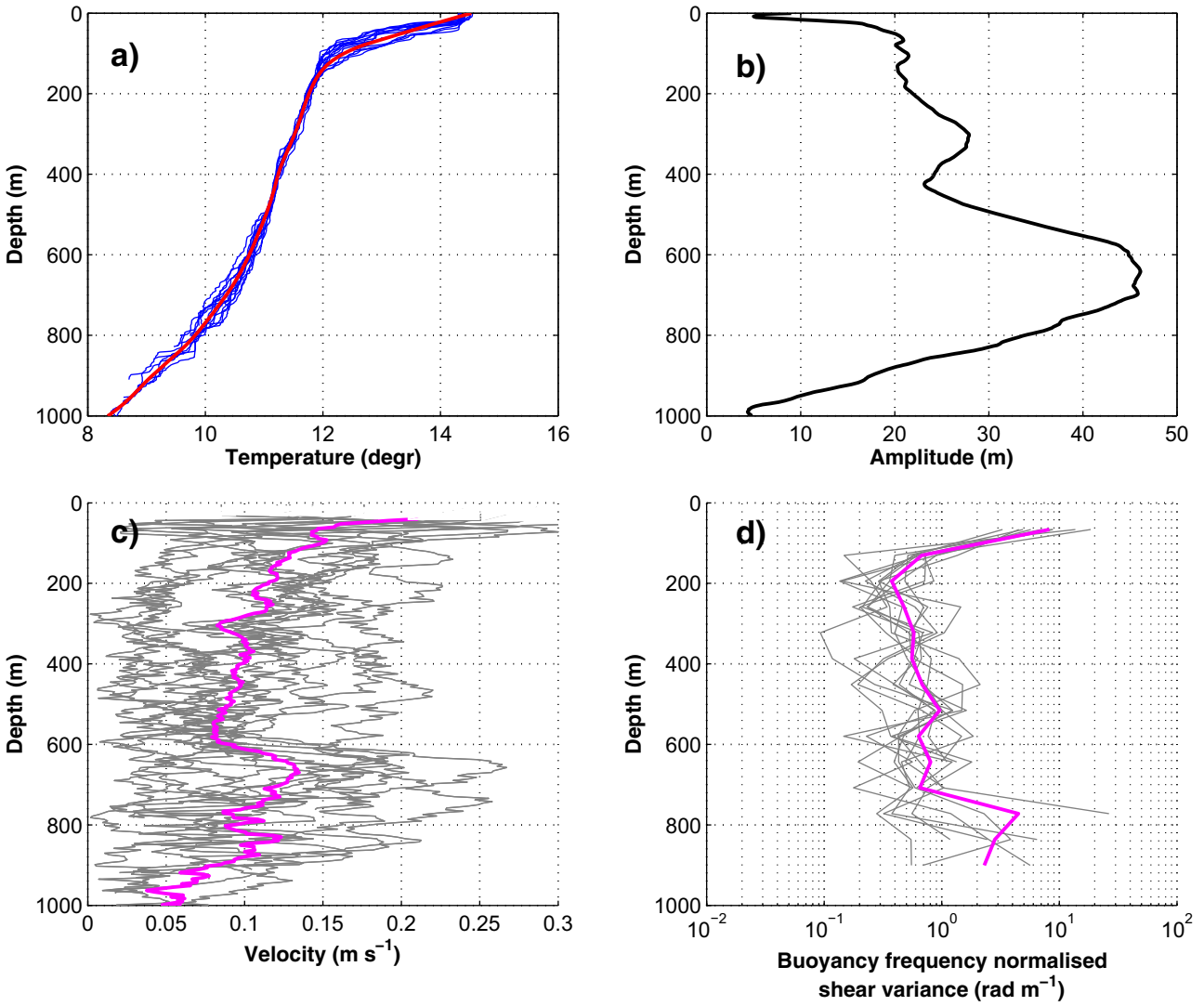

Figure 3. (a) Temperature profiles recorded at 14 "yo-yo" CTD stations (blue lines) along with the average temperature profile (red line). (b) Depth-dependent amplitude of isotherms deviation. (c) Horizontal velocity profiles recorded by LADCP (grey lines) and their mean profile (magenta line). (d) Distribution of shear variance. All profiles are shown in grey and the magenta line depicts their average.

The mean profile of $U(z)$ is presented in Figure 3c (magenta line). It shows the speed maximum at the free surface as well as a secondary local maximum at the depth of 680 m which coincides with the position the maximum vertical displacement and a broad region of elevated currents between 600 and 800 m, produced presumably by the action of internal waves.

As a proxy measure for the relative strength of diapycnal mixing, we follow the method of *Polzin et al.* [2002] in computing the buoyancy-normalized LADCP shear in overlapping segments (50% overlap), each of 128 m in vertical extent. The spectra for each segment were then integrated between vertical wavelengths of 25–128 m, to give 14 profiles of shear variance, a property that scales with the diapycnal eddy diffusivity. The time-averaged vertical profile of the shear variance (Figure 3d) demonstrates a relative sevenfold increase below 700 m depth, with a broad maximum at 780 m. The necessary segmentation of the data results in loss of vertical resolution in comparison with temperature or velocity profiles, but nevertheless a consistent deep maximum in fine-structure-derived vertical mixing is clearly apparent.

Intensification of vertical and horizontal motions in the layer between 500 and 800 m depth, classified above as a consequence of internal waves action is confirmed by Figure 4, where the temperature and eastward horizontal velocity profiles recorded at all 14 CTD stations are shown as time series. Both plots reveal

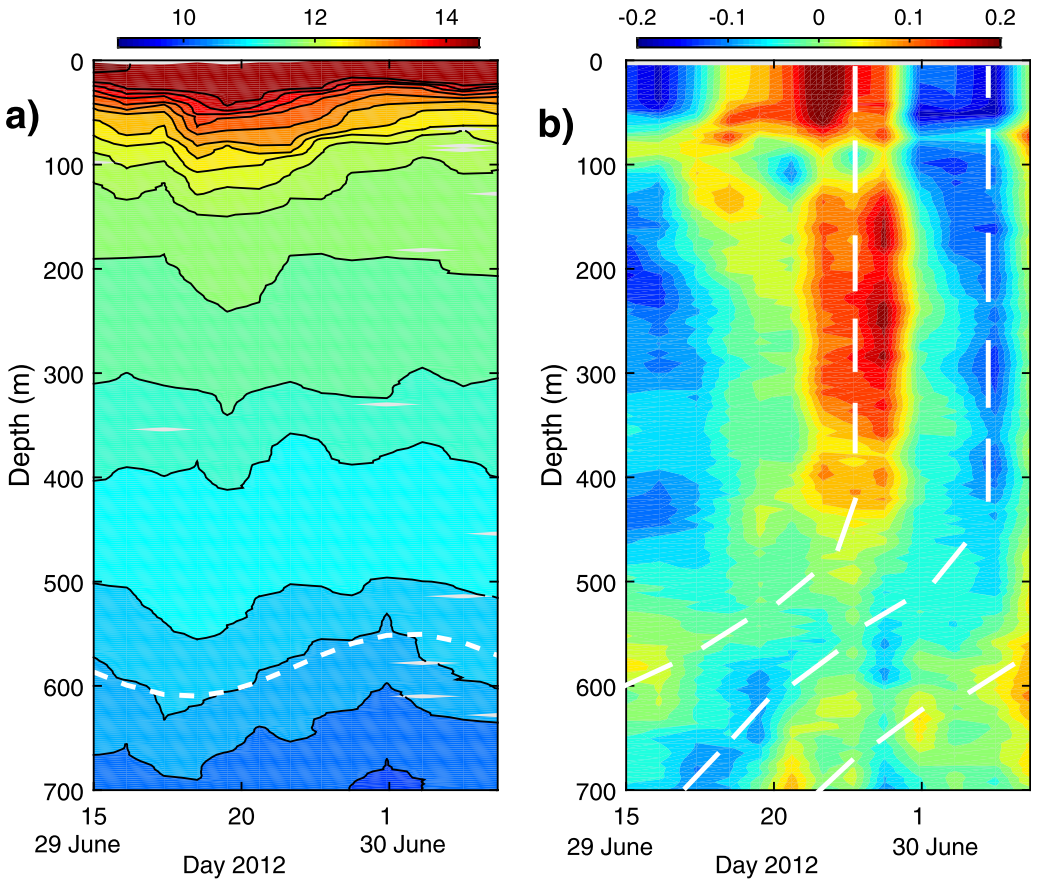

Figure 4. (a) Temperature (°C) and (b) eastward horizontal velocity (m s^{-1}) recorded at the "yo-yo" CTD station and presented as time series. Dashed lines in Figure 4b show upward propagation of the tidal beam phase, as it is schematically shown in Figure 1c.

semidiurnal periodicity of the recorded signals, with strong baroclinic contributions (note the intensification of horizontal currents and vertical oscillation in the surface 200 m, which is consistent with Figure 3). The most interesting feature of Figure 4a is clear evidence of intensive semidiurnal periodicity below 500 m depth (white dashed line in panel a) with relatively quite background between 500 and 200 m.

Horizontal currents also reveal semidiurnal periodicity, most clearly seen in the surface 400 m layer. At first glance, this periodicity can be attributed to barotropic tidal motions. However, weakening of the tidal signal below 400 m and its vertical intermittency in the deep layers suggests that there should also be a strong contribution of a baroclinic signal. Moreover, analyzing the relative location of minima and maxima of the velocity pattern in space and time one can conclude that Figure 4b can be treated as evidence of evolution of a baroclinic tidal beam with its phase moving upward (as it is presented in Figure 1c). Co-phase segments of the beam are marked in Figure 4b by white dashed lines. It is interesting to note that similar features have been found also in the model output which was applied in this paper to replicate the tidal dynamics in the canyon area. The results of modeling are discussed in the next section.

In order to bring more clarity to the interpretation of these relatively sparse observations and to understand the reasons for apparent internal wave energy and vertical mixing intensification in the deep part of the canyon, a series of numerical experiments was conducted.

3. Model Results

The fully nonlinear nonhydrostatic MITgcm was used to model internal tides in the canyon and the surrounding area (see Figure 2b). In the main part of the model domain, the horizontal and vertical resolutions were 100 and 10 m, respectively. In order to avoid any spurious boundary reflections, an exponentially increasing horizontal grid step near the lateral boundaries was used that guaranteed an accurate numerical

solution within the internal model domain without any signals reflected from the boundaries during at least 10 tidal cycles.

The tidal forcing was set in the model by a tidal potential added to the right hand side of the momentum balance equations. Its intensity was chosen using TPXO8.0 [*Egbert and Erofeeva*, 2002] in such a way as to reproduce tidal velocities recorded by moored ADCP current meters deployed during D376 that have shown the predominance of semidiurnal M2 tidal harmonic [*Vlasenko et al*., 2014]. Spatial distribution of tidal ellipses is shown in Figure 2d. A vertical stratification was introduced into the model after setting the tidal forcing for a homogeneous fluid. The temperature and salinity profiles were taken from the direct CTD measurements at the yo-yo station.

The Richardson number-dependent parametrization for vertical viscosity ν and diffusivity κ introduced in *Pacanowski and Philander* [1981] was used:

$$\nu=\frac{\nu_0}{(1+\beta \mathrm{Ri})^n}+\nu_b, \quad \kappa=\frac{\nu}{(1+\beta \mathrm{Ri})}+\kappa_b.$$

Here Ri is the Richardson number, $\mathrm{Ri}=N^2(z)/(u_z^2+v_z^2)$, u and v are the components of horizontal velocity; $N(z)$ is the buoyancy frequency $N^2(z)=-g/\rho(\partial\rho/\partial z)$ in which g is the acceleration due to gravity and ρ is the water density; $\nu_b=10^{-5}\,\mathrm{m^2\,s^{-1}}$ and $\kappa_b=10^{-5}\,\mathrm{m^2\,s^{-1}}$ are the background viscosity and diffusivity, respectively; $\nu_0=1.5\cdot 10^{-2}\,\mathrm{m^2\,s^{-1}}$, $\beta=5$, and $n=1$ are the adjustable parameters. Such a parametrization increases ν and κ in areas where the Richardson number is small. The horizontal viscosity and diffusivity were set to a constant value of $0.5\,\mathrm{m^2\,s^{-1}}$. More details on the model initialization and input parameters can be found in *Vlasenko et al*. [2014].

The principal question to be addressed by the modeling efforts is to identify the cause of the highly energetic internal wave activity in the center of the canyon below 500 m depth. The modeling evidence of this intensification in deep water is seen in Figure 5 where the amplitude of the model-predicted horizontal velocities

$$U_{\max}(x,y,z)=\sqrt{u_{\max}^2(x,y,z)+v_{\max}^2(x,y,z)}.$$

is presented. Here $u_{\max}(x,y,z)$ and $v_{\max}(x,y,z)$ are amplitudes of the eastward and northward velocities found over one tidal cycle at the position (x,y,z).

Nine horizontal slices of the velocity $U_{\max}$ at depths of between 300 and 700 m presented in Figure 5 reveal quite a curious tendency. In the surface layers, i.e., shallower than 500 m, the wave energy is mostly concentrated at the periphery of the canyon corresponding to the shelf break area. However, below this depth, the regions with high energy concentration are mostly located within the center of the canyon, not around its edge. This finding is consistent with the observational profiles shown in Figures 3b and 3c that reveal the energy maximum at approximately 700 m depth recorded at the CTD station in the middle of the canyon.

Such a focusing of internal wave energy in the canyon's center can be explained in terms of a superposition of several tidal beams generated at the shelf edge on the periphery of the canyon and radiating downward toward the center of the canyon, as it is shown in Figure 1c. Indeed, analysis of the bottom steepness (2) has shown that $\alpha \ll 1$ in the surrounding shelf area, but $\alpha > 1$ in the central part of the canyon, see Figure 6a. The red zones here, situated along the shelf break, separate the areas of subcritical shelf from the supercritical abyssal part of the canyon.

It is important to note that the positions of the potential generation cites of tidal beams (as sectors A-C shown in Figure 1c) correlate very well with the locations of the internal body force (IBF) introduced by *Baines* [1982] for quantification of the tidal energy conversion. In a two-dimensional (x,z) case, the IBF reads:

$$F=\rho Q z\frac{N(z)^2}{\omega}\left(\frac{1}{H(x)}\right)_x.$$

Here Q is water discharge produced by tides and ρ is the reference density. Being integrated from the surface to the bottom, this formula gives an overall efficiency of the internal tide generation for the whole water column, $\Phi=\int_{-H}^{0} F dz$. In a three-dimensional case (x,y,z), the vertically integrated IBF in every point is

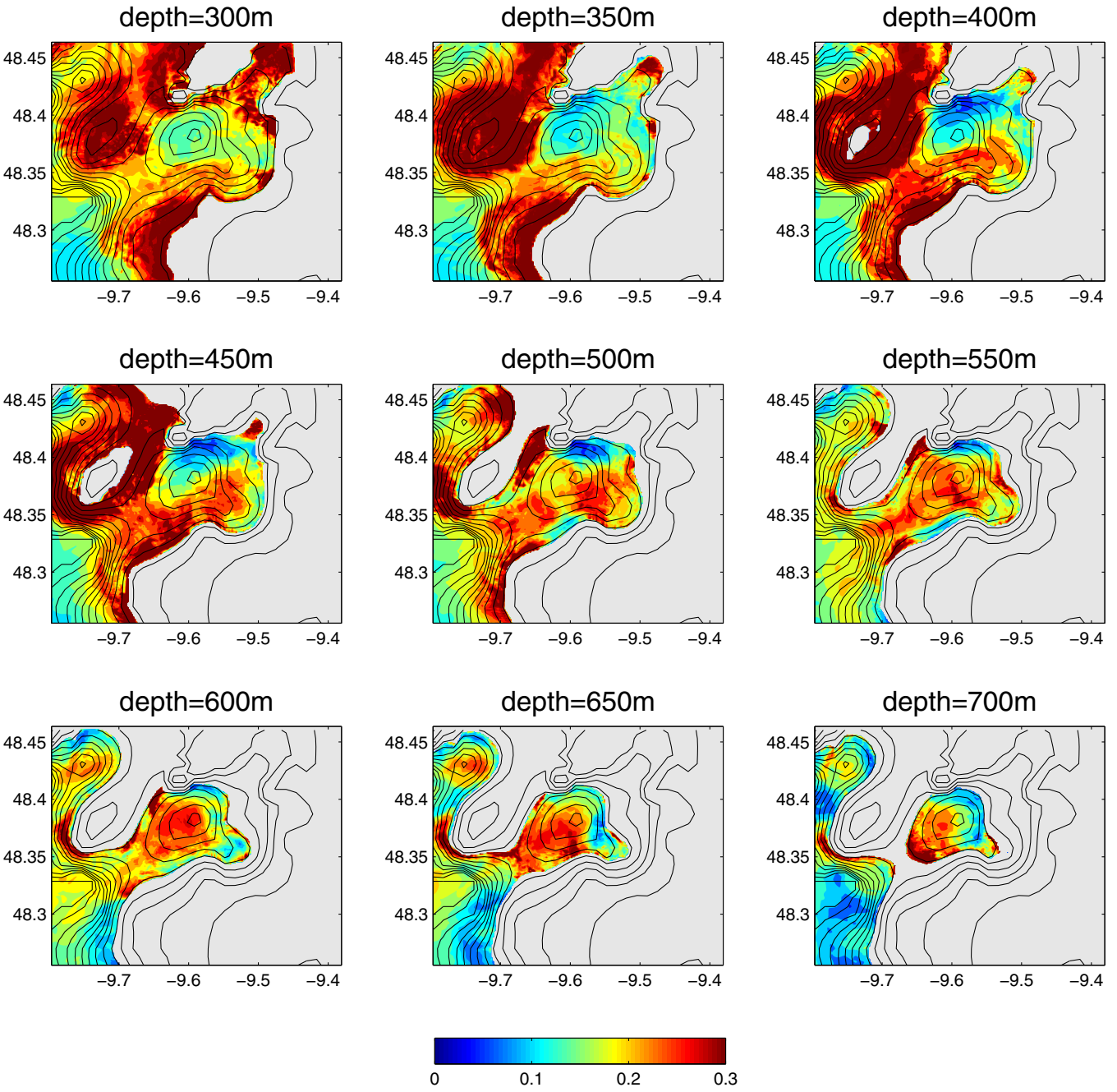

Figure 5. Horizontal distribution of the amplitudes of horizontal velocity at different depths.

calculated using the discharge and the derivative $\partial(1/H)/\partial l$, where l in the direction of the depth gradient, as shown in formulae (2). The spatial distribution of the vertically integrated IBF Φ shown in Figure 6b was calculated for the stratification presented in Figure 1a and the tidal forcing depicted in Figure 2.

Figure 6 a demonstrates that the main part of the canyon topography is supercritical for semidiurnal internal tidal waves with the maximum IBF concentrated around the canyon rim. As a result, according to theory [*Vlasenko et al*., 2005], the internal tide in the canyon should take a form of tidal beams generated at the shelf break around the canyon periphery which radiate downward toward the center of the canyon, as is shown in the scheme depicted in Figure 7. Bearing in mind that the canyon head has a near-circular shape, it is expected that it can function like an optical lens focusing wave energy into its center. Evidence for that interpretation is presented in Figure 8a for the vertical cross section depicted in Figure 2b by a white line.

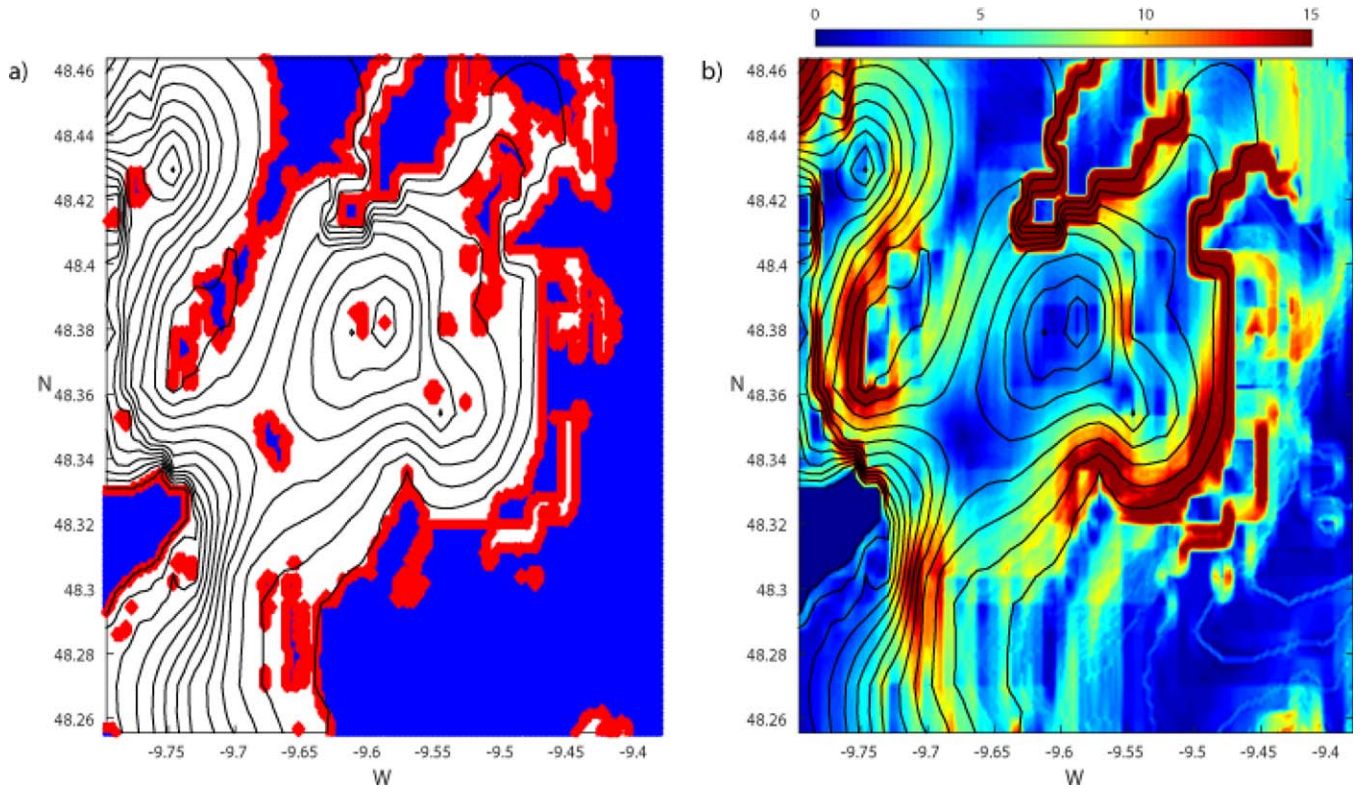

Figure 6. (a) Spatial distribution of parameter α: blue areas $\alpha < 1$, red stripes $\alpha = 1$, and clear areas with $\alpha > 1$. (b) Positions of vertically integrated internal body force Φ ($m^2 s^{-2}$).

Three tidal beams can be identified in Figure 8a (the characteristic lines, equation (1), are shown here by thin white lines). The tidal beam *a-b-c* is generated at the shelf break point, at *b*, and propagates downward along characteristic line *b-c*. The internal wave beam pattern, resembling a St.Andrews cross, is generated at the saddle point *e*. The tidal energy propagates from this point along four characteristic lines, *e-g*, *e-d*, *e-h*, and *e-f*. It is interesting and relevant to note that the two tidal beams generated at the opposite sides of the canyon, viz. *b-c* and *e-f* meet in the center of the canyon in the layer between 600 and 800 m depths which is consistent with the position of the deep water maxima in vertical displacement, horizontal velocity, and shear variance seen in Figure 3d.

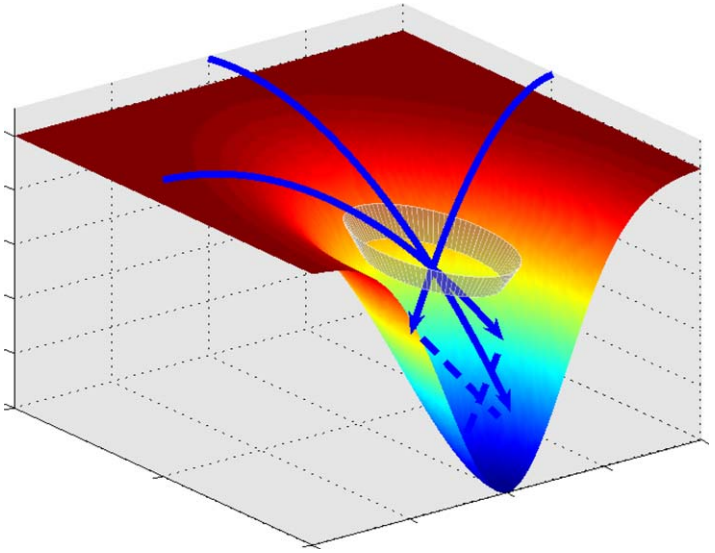

Figure 7. Scheme of interference of tidal beams in the center of an idealized canyon with formation of a baroclinic eddy.

Observational evidence of the tidal beam can also be found in Figure 4b where the northward horizontal velocity recorded at the yo-yo station is presented as a time series. It correlates well with Figure 9d where similar signal, predicted by the MITgcm at the position of the yo-yo station, is presented. Consistency of both patterns is obvious, although the observational one is less contrasted and more noisy. Both

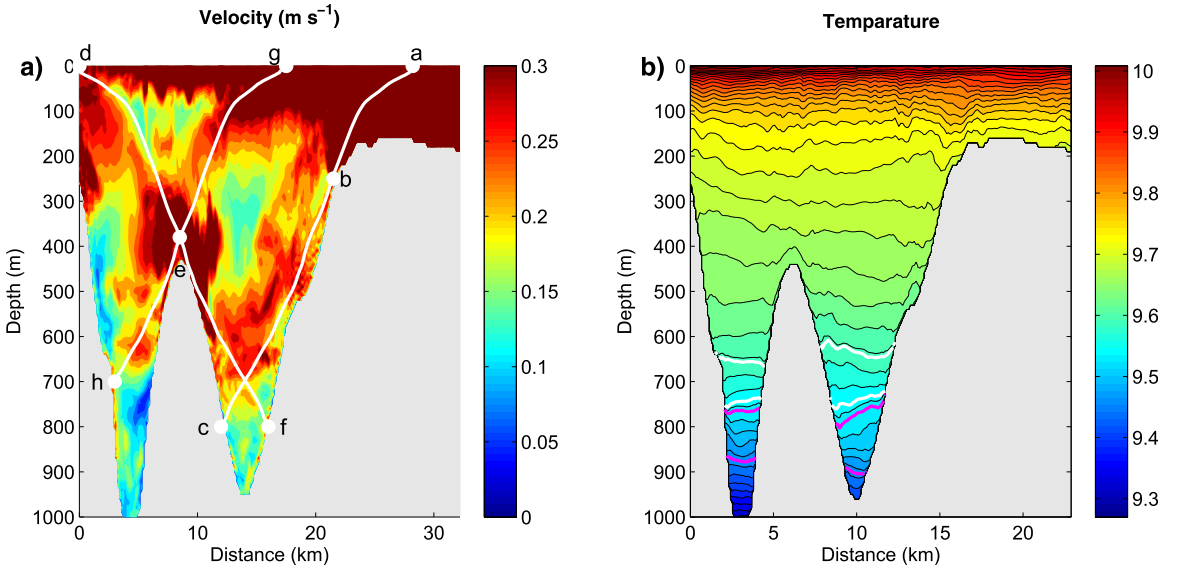

Figure 8. (a) The largest values of horizontal velocity calculated for the cross section shown in Figure 2a. White contours depict characteristic lines (1). (b) Average temperature distribution with upper white contour representing isotherm 10.55°C and the lower one 10.1°C. Similar values for two magenta isolines are 10.0°C and 9.3°C.

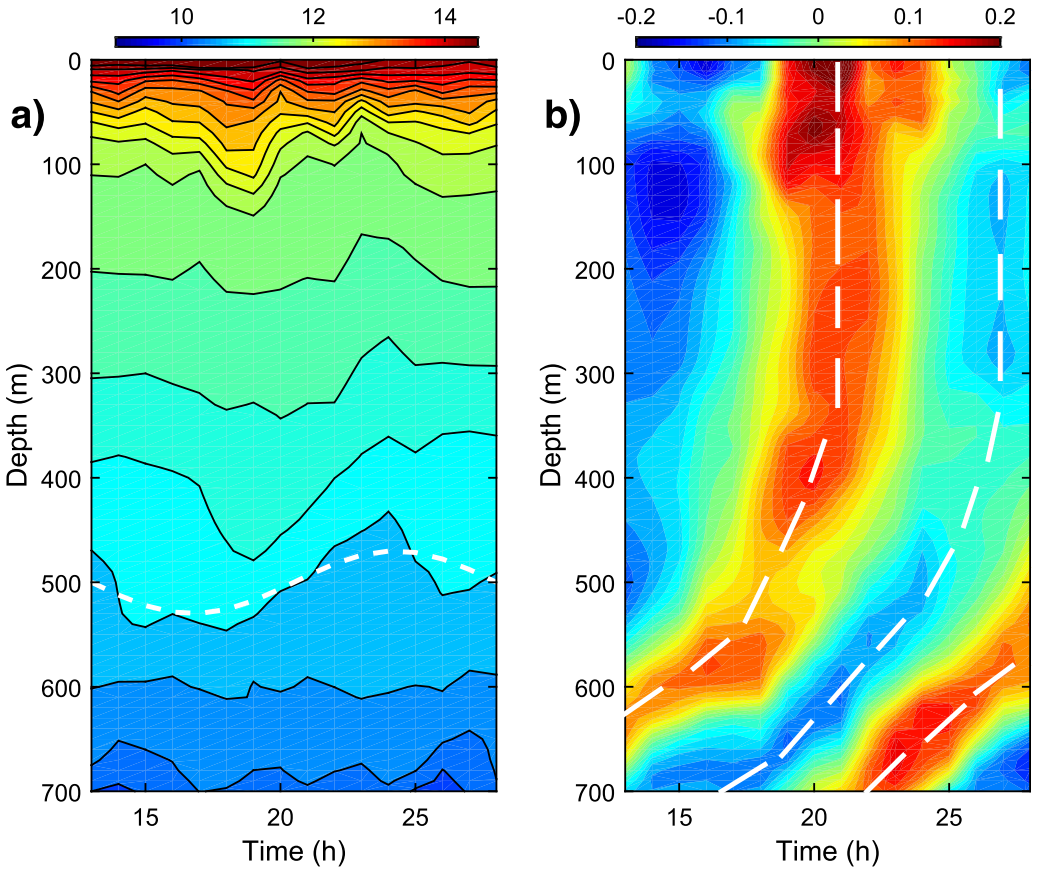

Figure 9. Model-predicted (a) temperature (°C) and (b) eastward horizontal velocity (m s $^{-1}$) for the position of the "yo-yo" CTD station presented as time series. Dashed lines in the velocity Figure 9b show upward propagation of the tidal beam phase, as it is schematically shown in Figure 1c.

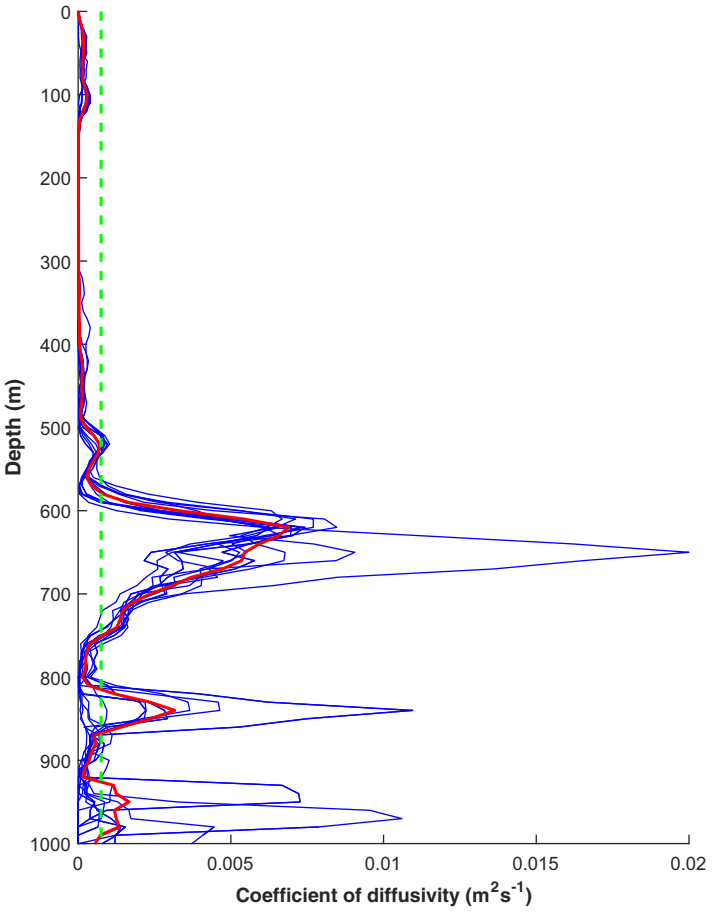

Figure 10. The coefficient of vertical diffusivity κ at the position of the yo-yo station calculated using the *Pacanowski and Philander* [1981] parametrization. Blue lines show instant profiles for the moments of yo-yo sampling, and the red line depicts an average profiles. Dashed line depicts the depth-averaged value, 7.5×10^{-4} ($m^2 s^{-1}$).

plots reveal upward propagation of the wave phase (shown by dashed white lines in Figures 4b and 9b), which can be treated in terms of the tidal beam evolution schematically presented in Figure 1c.

Model-predicted vertical displacements of the isotherms below 400 m depth are a bit larger than those recorded in situ (compare Figures 4a and 9a), although both plots demonstrate evidence of semidiurnal periodicity (find white dashed lines) and relatively "calm" internal wave activity in the intermediate layers (between 150 and 350 m).

As seen from Figure 6, similar conditions of the energy focusing discussed above, i.e., position of subcritical and supercritical areas, are valid also for many other cross sections passing through the center of the canyon. In other words, the tidal energy is converted at many particular areas around the canyon periphery, and is then radiated toward its center and accumulated there at the depths of between 500 and 800 m, as is observed in the CTD/LADCP analysis.

Such focusing of wave energy in the canyon's center should increase the associated level of local water mixing there, since energy cannot accumulate indefinitely. Elevated shear variance is testament to greater elevated mixing at depth (Figure 3d). Model results demonstrate a similar increase of vertical diapycnal mixing. Figure 10 shows that the coefficient of vertical diffusivity κ in the center of the canyon calculated using the Richardson number-dependent parametrization [*Pacanowski and Philander*, 1981] increases from the background level $\kappa_b = 10^{-5}$ m^2 above 500 m depth up to 10^{-2} m^2 in the layer from 600 to 800 m depth where the tidal beam meet in the center of the canyon. This dramatical increase suggests strong diapicnal mixing in the place of tidal beam focusing. As a result of intensified local diapycnal mixing, a quasi stationary density (temperature) gradient is formed across the canyon, as shown in Figure 8b (the same cross section as in Figure 8a). Convergence and divergence of isotherms at the depths of between 500 and 900 m is clearly seen here from two pairs of isotherms colored in white and magenta. Initially (before the model run), the distance between both (parallel) isolines was equal to 100 m: the upper and lower "white" isotherms were initially at depths of 650 and 750 m, respectively; the upper and lower "magenta" isotherms were initially at depths of 800 and 900 m. After 10 cycles of tidal action, the distance between the two groups of isotherms was modified: at some positions, they converged, and at others they diverged. Figure 11 shows the difference between isotherms initially centered at 700 m (Figure 11a) and at 850 m (Figure 11b). It is interesting that the convergence and divergence of isolines is opposite for the two depth pairs, Figures 11a and 11b.

The formation by diapycnal mixing of quasi-stationary horizontal pressure gradients suggests the existence of geostrophically balanced baroclinic eddies. A quasi-stationary eddy is clearly seen in Figure 12 in the velocity vector fields at depths of 450, 600, and 700 m. It was obtained by subtraction of the barotropic tidal

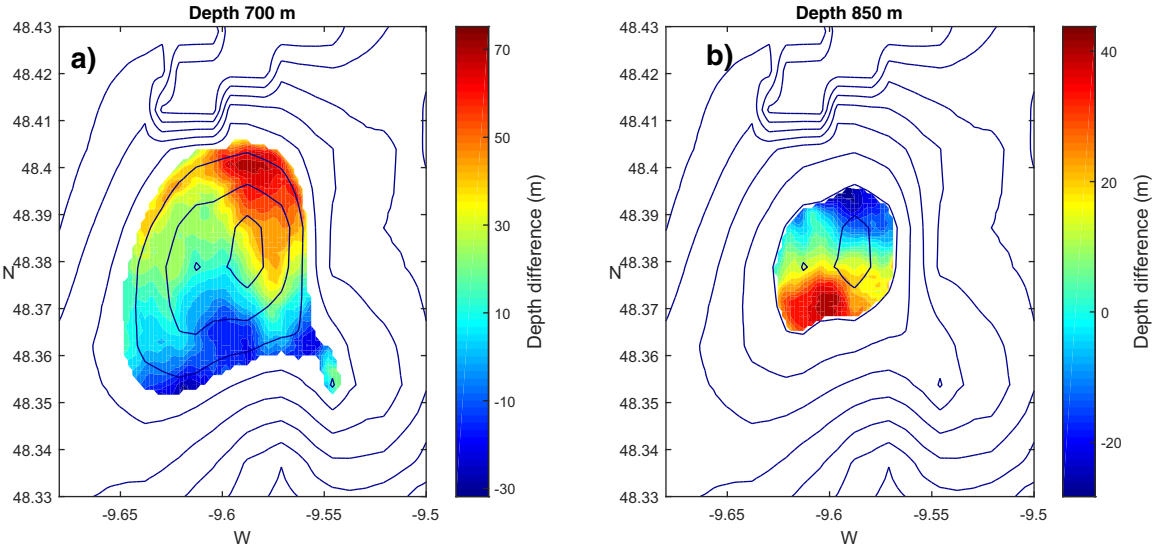

Figure 11. (a) The distance between isotherms shown in Figure 8b in white. (b) The distance between isotherms shown in Figure 8b in magenta.

flow (at each point it was found as an average value of the velocity through the whole water column from surface to the bottom) and by averaging of all fields over several tidal periods in order to exclude periodic tidal motions and to reduce noise. The eddy around the topography bank is seen at a depth of 450 m where the tidal beam is still located close to the canyon flank and the shelf edge. However, vertical motions are absent in the center of the canyon at this depth (450 m). According to the findings presented above, the

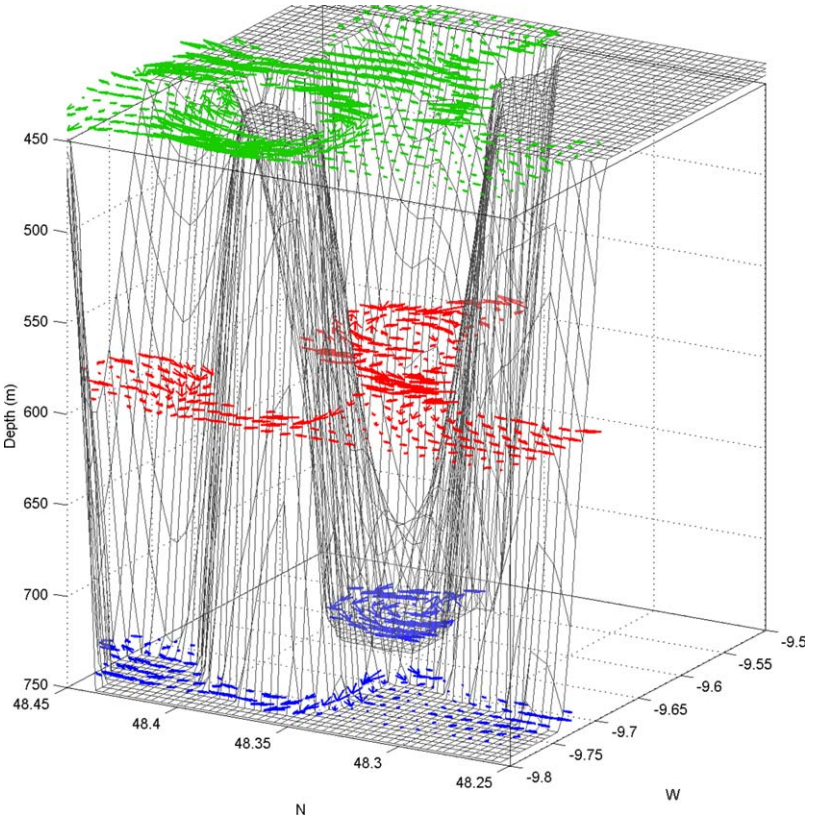

Figure 12. Velocity vectors of the model-predicted baroclinic eddy generated inside the canyon. The currents are shown at depths 450 m (green arrows), 600 m (red arrows), and 700 m (blue arrows).

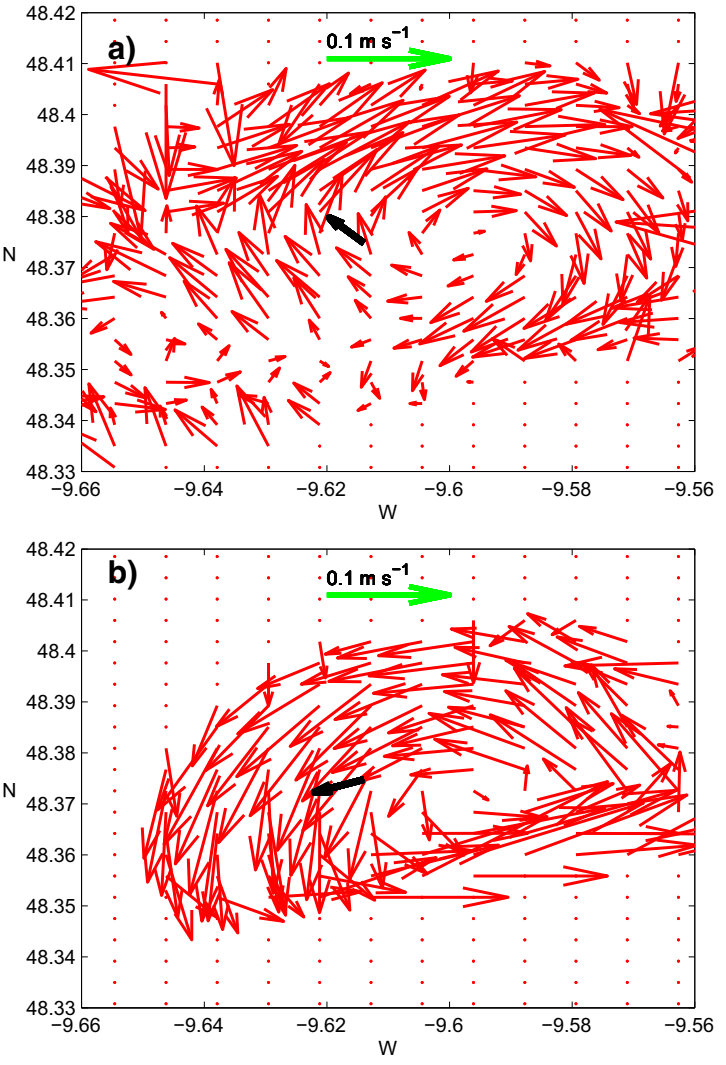

Figure 13. Model-predicted anticyclonic and cyclonic eddies at the depths of (a) 600 m and (b) 750 m. Average baroclinic currents recorded by LADCP at the same depths are shown by black arrows.

tidal energy is mostly concentrated beneath 450 m and in the center of the canyon. Here a baroclinic eddy with anticyclonic rotation at 600 m depth and cyclonic rotation at 700 m depth is clearly seen.

Note that the correct choice of the model parameters for the turbulent closure that produces an adequate eddy pattern is not always possible without validation of the model output against observational data. In our case, we used observations by *Inall et al.* [2000] conducted over the Malin Sea continental slope adjacent to the considered here area. Direct in situ measurements of the background turbulence allowed them to quantify the vertically integrated coefficient of turbulent diffusion in the range $(5\text{-}12)\times10^{-4}$ (m^2s^{-1}). Integration of the vertical profile of diffusivity shown in Figure 10 produced by the model returns the value of 7.5×10^{-4} (m^2s^{-1}) (shown by a dashed line) which is well inside of the in situ observed range.

To find observational evidence of the predicted baroclinic eddy generated in the middle of the canyon, the following analysis of the LADCP data was performed. First, the barotropic velocities U_j^{bar} and V_j^{bar} were found by averaging of the instant velocity profiles:

$$U_j^{bar}=\frac{1}{H_j}\int_0^{H_j}u_j(z)dz;$$

$$V_j^{bar}=\frac{1}{H_j}\int_0^{H_j}v_j(z)dz.$$

$j=1,2,3,\cdots,14$. Second, the barotropical tidal signal was removed from the sampling data using the following procedure:

$$u_j^{int}=u_j-U_j^{int};$$

$$v_j^{int}=v_j-V_j^{int},$$

It is clear that the remaining baroclinic signals u_j^{int} and v_j^{int} contain both mean currents and internal waves. They are also not free from a random signal that always is present in any observational data set. In order to

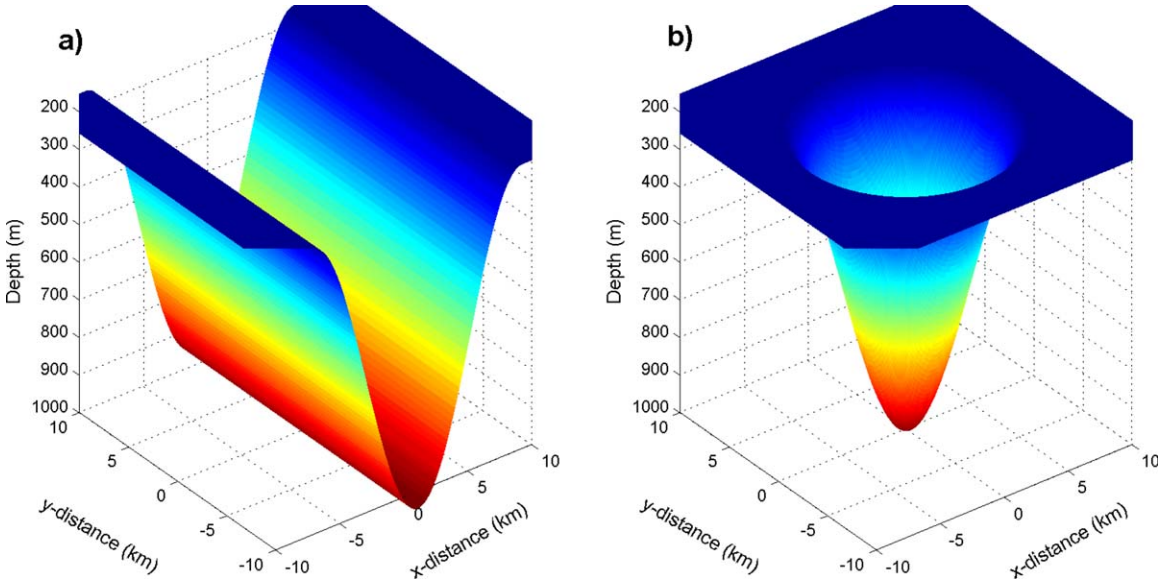

Figure 14. Bottom topography of idealized (a) two-dimensional and (b) three-dimensional canyons.

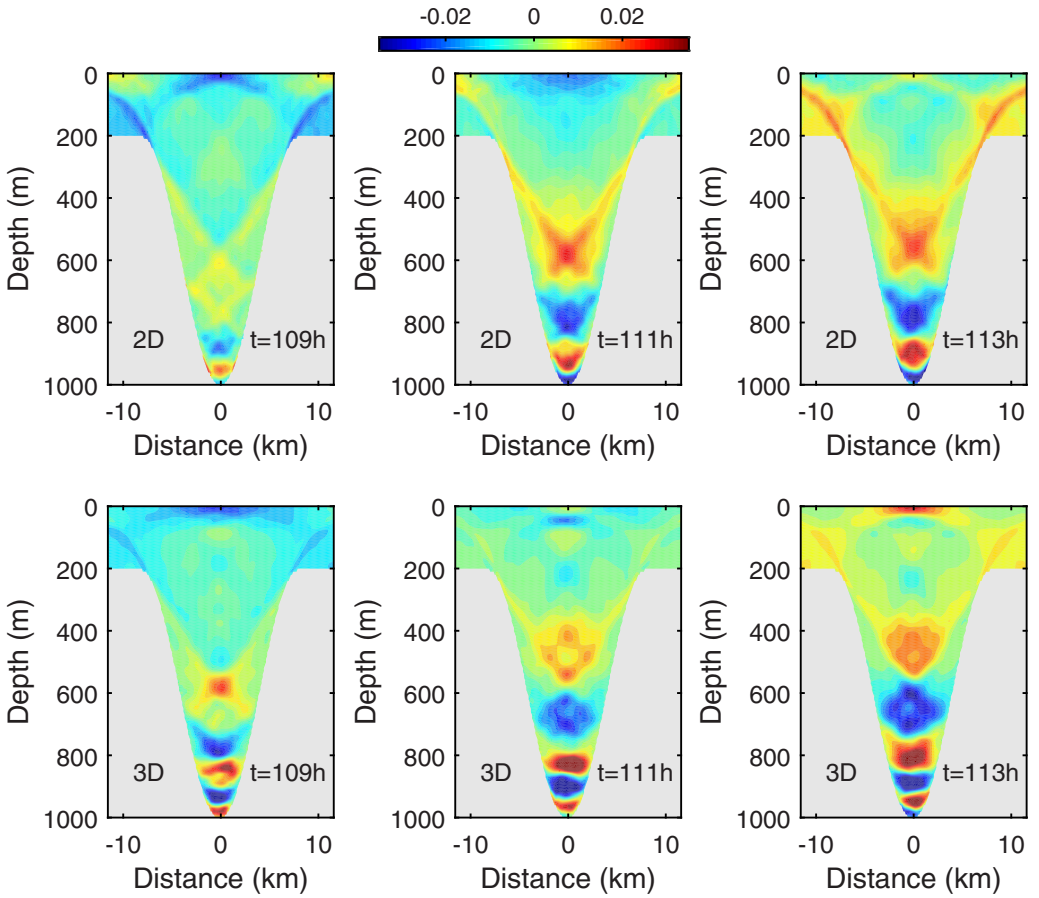

Figure 15. Instant horizontal velocities in the (top) two-dimensional and (bottom) three-dimensional canyons. The time after beginning of the numerical experiment is shown in the bottom right corner of each plot.

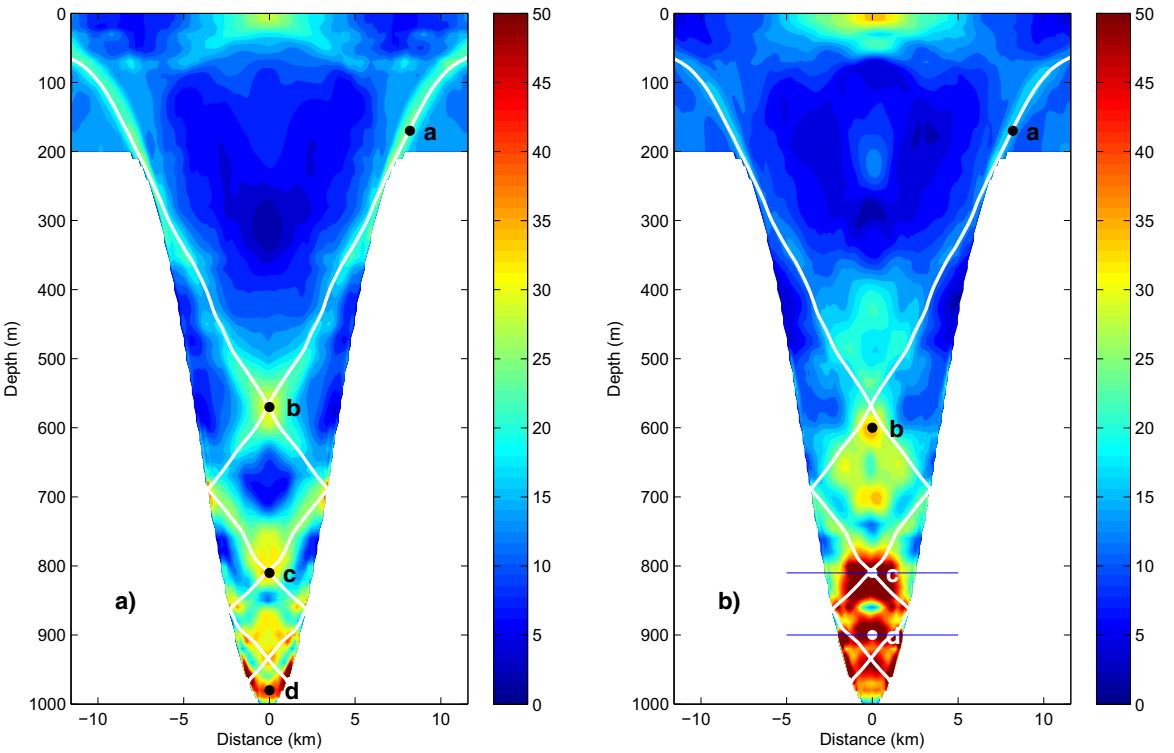

Figure 16. Amplitude of the baroclinic tidal energy (J m^{-3}) in (a) two-dimensional and (b) three-dimensional canyons. White contours depict characteristic lines (1).

reduce the noise, average vertical profiles of both components were calculated as follows: $u^{\mathrm{int}}(z)=1/14\sum_{j=1}^{14} u_j^{\mathrm{int}}(z)$ and $v^{\mathrm{int}}(z)=1/14\sum_{j=1}^{14} v_j^{\mathrm{int}}(z)$. In addition, vertical averaging of $u^{\mathrm{int}}(z)$ and $v^{\mathrm{int}}(z)$ in 100 m thick layers with centers at depths 600 and 750 m was conducted. The resulting vectors along with the model-predicted vectors are presented in Figures 13a and 13b. Looking at the averaged velocity vectors, one can discern a good consistency. It seems that the direction of the black arrows in Figures 13a and 13b is consistent with that predicted by the model, i.e., the anticyclonic and cyclonic rotation in depths 600 and 750 m layers, respectively. This can be considered as further evidence that tidal energy focusing in the center of the canyon is responsible for the formation of baroclinic eddies there.

4. Two-Dimensional Versus Three-Dimensional Focusing

The importance of three-dimensional effects in focusing of baroclinic tidal energy in the center of a circular canyon (as shown in Figure 7) can be demonstrated and quantified more accurately by comparing three-dimensional (3-D) and two-dimensional (2-D) simplified cases. In doing so, a series of numerical experiments were conducted for two idealized canyons, shown in Figure 14. The shape of both canyons in the x direction was the same, i.e., $H(x)=H_0+H_m\cos^2(\pi x/2l)$, although in a 2-D case, the canyon was indefinitely long in the y direction to exclude influence of the y derivatives, but its 3-D counterpart has circular form, see Figure 14b. The parameters of the bottom topography were taken realistic, i.e., $H_0=200$ m, $H_m=800$ m, and $l=7.5$ km. The buoyancy frequency in this series of experiments was taken according to profile shown in Figure 1a, but the intensity of the tidal forcing was taken 10 times weaker than in section 3 in order to reduce the influence of nonlinear terms and to show the effect of tidal energy focusing more clearly.

Two systems of tidal beams are generated at either sides of both canyons. In Figure 14, they are presented as a series of instant horizontal velocity fields both for 2-D (top) and 3-D (bottom) canyons. Tidal energy is radiated upward and downward from the shelf edges propagating in narrow bands along characteristic lines (1). Downward propagating tidal beams meet in the center of the canyons at the depth of about 550 m and amplify each other creating a spots of high tidal activity. Propagating further downward, the

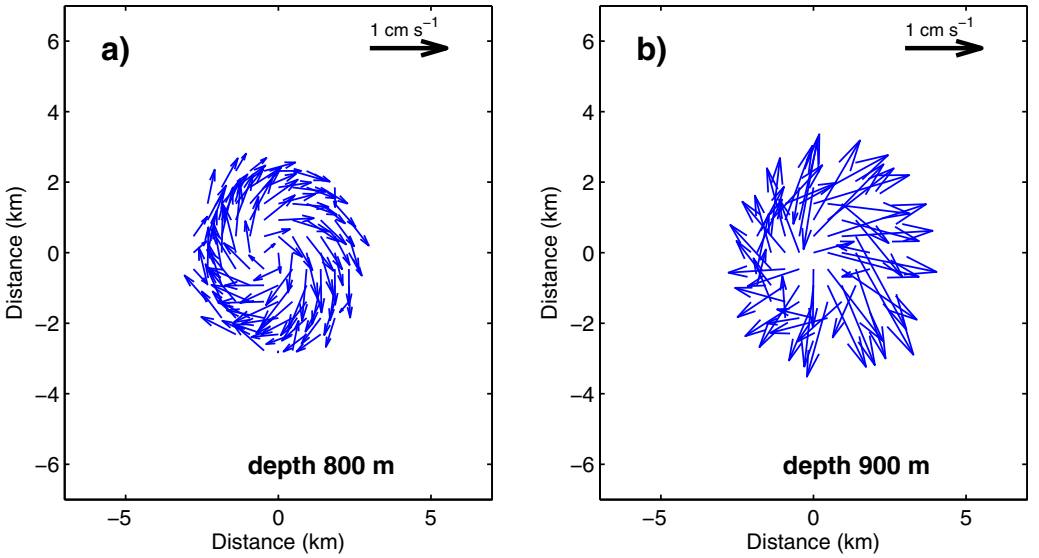

Figure 17. Model-predicted anticyclonic eddies in an ideal circular canyon.

tidal beams experience multiple reflections from the canyon flanks and produce amplification of tidal energy in the canyon centers. As a result of narrowing cross section of canyons down to the deep, the intensity of tidal motion increases. This effect is clearly seen in all six plots presented in Figure 15.

The comparison analysis of the top and bottom plots shows that the structure of the wave fields in two-dimensional and three-dimensional canyons is a bit different. Note also quite a different level of intensity of baroclinic motions in both canyons. They look weaker near the surface in the 3-D case, but stronger in its deep part.

In order to quantify the difference more accurately, the amplitude of the baroclinic tidal energy $E=0.5\rho(u^2+v^2+w^2+N^2\xi^2)$ was calculated (here u, v, and w are the components of the velocity vector, N is the buoyancy frequency, ξ is isopicnal displacement, and ρ is the water density). The amplitude values of energy density are presented in Figure 16 both for 2-D and 3-D canyons. Four control points with maximum of local tidal energy have been chosen for the comparative analysis: the point **a** near the shelf break where tidal beams are generated, points **b** and **c** in the deep part where the beams intersect, and point **d** with the highest level of concentration of baroclinic tidal energy (near the bottom). The appropriate values of the energy density were 24, 31, 32, and 43 J m^{-3} for the 2-D canyon and 16, 36, 61, and 50 J m^{-3} for the 3-D one. From this series of experiments, it is clear that a 2-D canyon is more efficient in terms of the tidal energy conversion demonstrating 1.5 larger value of baroclinic tidal energy at the shelf break. At the same time, the intensity of the baroclinic tidal motions in the deep is much higher in the three-dimensional case. In fact, the 3-D canyon works as an optical lens focusing the tidal energy from all directions into a focal center. Even though the tidal beams generated at the shelf break of the 3-D canyon are 1.5 times weaker than in a 2-D case, the 3-D focusing provides 2 times larger density of baroclinic tidal energy in the deep part of the canyon than its 2-D counterpart.

The increase of baroclinic tidal energy in the deep part of the 3-D canyon compared to that in surface layers results in larger level of diapicanal mixing and formation of stronger geostrophically adjusted eddies near the bottom. This fact is clearly seen in Figure 17 where vectors of the velocity fields averaged over one tidal cycle at depths 800 and 900 m are presented. These two sections coincide with the positions of the maximum of tidal energy concentration depicted in Figure 16b by letters **c** and **d**. Both patterns demonstrate evidence of an anticyclonic eddy with the velocities at the level of 1 cm s^{-1}. Note, however, that the currents near the bottom at the depth of 900 m on average are 2 time stronger than that at 800 m depth. This is consistent with Figure 16b which demonstrates higher energy concentration near the bottom.

5. Discussion and Conclusions

Submarine canyons are common bathymetric features at many of the world's shelf edge regions. They can trap internal wave energy holding it toward the head of canyons in a converging wave guide that can lead

to a high level of turbulent mixing there. This mechanism was discussed by *Baines* [1983], *Gardner* [1989], Gordon and Marshall [1976], and *Hotchkiss and Wunsch* [1982]. Note, however, that the aforementioned papers appeal predominantly to a two-dimensional concept of this mechanism. In reality, one should operate with three-dimensional characteristic surfaces of a 3-D wave equation rather than with the characteristic lines of its 2-D counterpart. As a result of the three dimensionality, the tidal beams emanating from flanks of a concave topography can focus in its center producing a spot with high levels of internal wave energy and mixing. This paper deals with the three-dimensional aspects of this focusing mechanism.

The possibility of intensification of baroclinic tidal energy due to wave interference was recently reported in a number of theoretical papers. *Carter* [2010] analyzing model output for baroclinic tide in the Monterrey Bay region testified interference of internal waves generated at different sectors of the bay. It was found that the model predicted up to 5 times increase of the baroclinic tidal flux close to the Monterrey canyon axis located in the center of the bay. It was hypothesized there that the effect was created thanks to topographic focusing, although this fact was not clarified, specifically in terms of the beam-like structure of baroclinic tides or supercriticality of the bottom topography.

Similar effects of the interference of baroclinic tidal energy radiated from scattered multiple sources were also reported by *Rainville et al*. [2010] for the Hawaiian Ridge area. As distinct from the present study, mostly horizontal interference of the baroclinic tidal waves was studied; however, the effect of baroclinic tidal energy superposition was clearly demonstrated.

The most recent model study conducted by *Zhang et al*. [2014] for an idealized and supercritical for semidiurnal M2 tide canyon confirmed an asymmetry of internal tide near the canyon, which presumably is a consequence of the alongshore effects of propagating internal tidal wave. In fact, they focus mostly on resonant effects of internal tide generation in the canyon and its beam-like onshore propagation alongside explanation of the reasons for the asymmetry of tidal fields. With relevance to the present study, *Zhang et al*. [2014] reported the beam-like structure of baroclinic tides near the supercritical canyon, with a difference in deepward and shoreward structures, although their interference in the canyon area was not demonstrated.

Model output always allows us to study the process of wave focusing in detail; however, in reality, it is quite difficult to observe this effect in situ. For the Celtic Sea, we have found not only theoretical but also observational evidence of the baroclinic tidal energy focusing in the middle of the canyon. The measurements were conducted during D376 in the center of the Petite Sole Canyon situated at the shelf edge of the Celtic Sea (see Figure 2). CTD and LADCP data collected at a station in the middle of the canyon revealed large vertical oscillations of isotherms (up to 45 m, Figure 2b) and local maximum of horizontal currents (up to 0.12 m s^{-1}, Figure 3c) in the layer between 500 and 800 m.

The possibility of such an inherently three-dimensional focusing mechanism of baroclinic tidal energy was confirmed in a series of numerical experiments conducted using the MITgcm forced by M2 tidal harmonic. The high internal tidal activity in the deep part of the canyon (Figure 5) is treated here in terms of downward propagation and focusing of internal tidal beams generated at the shelf break. The specific circular shape of the canyon, coupled with the steep bottom topography below the shelf break (steeper than tidal beam) in all parts of the canyon create favorable conditions for the tidal energy focusing in the canyon's center, see Figure 7. Both observations and MITgcm simulations have also shown that the tidal energy focusing intensifies local diapycnal mixing (Figures 3d and 10), that can lead to formation of a baroclinic eddy below 450 m depth in the central part of the canyon, see Figure 12. Evidence consistent with the presence of the cyclonic and anticyclonic rotation in the canyon center was found also in in situ data.

The importance of the results is that the effect of the focusing of baroclinic tidal energy in 3-D configuration is quite a typical situation in many areas. This means that the results on the baroclinic tidal energy focusing reported here can have much wider application rather than just circular-shape canyons.

Acknowledgment
This work was supported by the Natural Environment Research Council grant FASTNEt (award NE/I030259/1). The used data are available at http://www.sams.ac.uk/fastnet.

References

Baines, P. G. (1982), On internal tide generation models, *Deep Sea Res., Part I*, *29*, 307–339.
Baines, P. G. (1983), Tidal motion in submarine canyons a laboratory experiment, *J. Phys. Oceanogr.*, *13*, 310–328.
Balmforth, N. J., and T. Peacock (2009), Tidal conversion by supercritical topography, *J. Phys. Oceanogr.*, *13*, 310–328.
Carter, G. S. (2010), Barotropic and baroclinic M_2 tides in Monterey Bay region, *J. Phys. Oceanogr.*, *39*, 1965–1974.

Egbert, G. D., and S. Y. Erofeeva (2002), Efficient inverse modeling of barotropic ocean tides, *J. Atmos. Oceanic Technol.*, *19*(2), 183–204.
Gardner, W. D. (1989), Periodic resuspension in Baltimore Canyon by focusing of internal waves, *J. Geophys. Res.*, *94*(C12), 18,185–18,194.
Gerkema, T., and H. van Haren (2012), Absence of internal tidal beams due to non-uniform stratification, *J. Sea Res.*, *74*, 2–7.
Gerkema, T., F. A. Lam, and L. R. Maas (2004), Internal tides in the Bay of Biscay: Conversion rates and seasonal effects, *Deep Sea Res., Part II*, *51*, 2995–3008.
Gordon, R. L., and N. F. Marshall (1976), Submarine canyons: Internal wave traps?, *Geophys. Res. Lett.*, *3*(10), 622–624.
Grimshaw, R., E. Pelinovsky, and T. Talipova (2010), Non-reflecting internal wave beam propagation in the deep ocean, *J. Phys. Oceanogr.*, *40*, 802–813.
Grimshaw, R. H. J., P. G. Baines, and R. C. Bell (1985), The reflection and difraction of internal waves from the junction of a slit and a half-space, with application to submarine canyons, *Dyn. Atmos. Oceans*, *9*, 85–120.
Hall, R. A., and G. S. Carter (2011), Internal tides in Monterrey Submarine Canyon, *J. Phys. Oceanogr.*, *41*, 186–204.
Hickey, B. M. (1995), Coastal submarine canyons, in *Topographic Effects in the Ocean: 'Aha Huliko'a Hawaiian Winter Workshop*, pp. 95–110, Univ. of Hawaii at Manoa, Honolulu.
Hotchkiss, F. S., and C. Wunsch (1982), Internal waves in Hudson Canyon with possible geological implications, *Deep Sea Res., Part A*, *29*(4), 415–442.
Inall, M. E., T. P. Rippeth, and T. J. Sherwin (2000), Impact of nonlinear waves on the dissipation of internal tidal energy at a shelf break, *J. Geophys. Res.*, 115(4), 8687–8705, doi:10.1002/2013JC009708.
Jachec, S. M., O. B. Fringer, M. G. Gerritsen, and R. L. Street (2006), Numerical simulation of internal tides and the resulting energetics within Monterrey Bay and the surrounding area, *Geophys. Res. Lett.*, *33*, L12605, doi:10.1029/2006GL026314.
Pacanowski, R. C., and S. G. H. Philander (1981), Parameterisation of vertical mixing in numerical models of Tropical Oceans, *J. Phys. Oceanogr.*, *11*, 1443–1451.
Petruncio, E. T., L. K. Rosenfeld, and J. D. Paduan (1998), Observations of the internal tide in Monterrey Canyon, *J. Phys. Oceanogr.*, *28*, 1873–1903.
Petruncio, E. T., J. D. Paduan, and L. K. Rosenfeld (2002), Numerical simulation of the internal tide in a submarine canyon, *Ocean Modell.*, *4*, 221–248.
Polzin, K., E. Kunze, J. Hummon, and E. Firing (2002) The finescale response of lowered ADCP velocity profiles, *J. Atmos. Oceanic Technol.*, *19*, 205–224.
Rainville, L., T. M. S. Jonston, G. S. Carter, M. A. Merifield, R. Pincel, P. F. Worcester, and B. D. Dushaw (2010), Interference pattern and propagation of the M_2 internal tide south of the Hawaiian Ridge, *J. Phys. Oceanogr.*, *40*, 311–325.
Shepard, F. P. (1974), "Internal waves" advancing along submarine canyons, *Science*, *19*, 195–198.
St. Laurent, L., S. Srtringer, C. Garrett, and D. Perrault-Joncas (2003), The generation of internal tides at abrupt topography, *Deep Sea Res., Part I*, *50*, 987–1003.
Vlasenko, V., and N. Stashchuk (2015), Internal tides near the Celtic Sea shelf break: A new look at a well known problem *Deep Sea Res., Part I*, *103*, 24–36, doi:10.1016/j.dsr.2015.05.003.
Vlasenko, V., N. Stashchuk, and K. Hutter (2005), Baroclinic tides: Theoretical modeling and observational evidence, 365 pp., Cambridge Univ. Press, Cambridge.
Vlasenko, V., N. Stashchuk, M. Inall, and J. Hopkins (2014), Tidal energy conversion in a global hot spot: On the 3-D dynamics of baroclinic tides at the Celtic Sea shelf break, *J. Geophys. Res. Oceans*, *119*, 3249–3265, doi:10.1002/2013JC009708.
Zhang, W. Z., T. F. Duda, and I. A. Udovychenkov (2014), Modeling and analysis of internal-tide generation and beamlike onshore propagation in the vicinity of shelfbreeak canyons, *J. Phys. Oceanogr.*, *44*, 834–849.
Zhao, Z., M. H. Alford, R. C. Lien, and M. C. Gregg (2012), Internal tides and mixing in submarine canyon with time-varying stratification, *J. Phys. Oceanogr.*, *42*, 2121–2142.